Journal of Materials Chemistry C

Accepted Manuscript

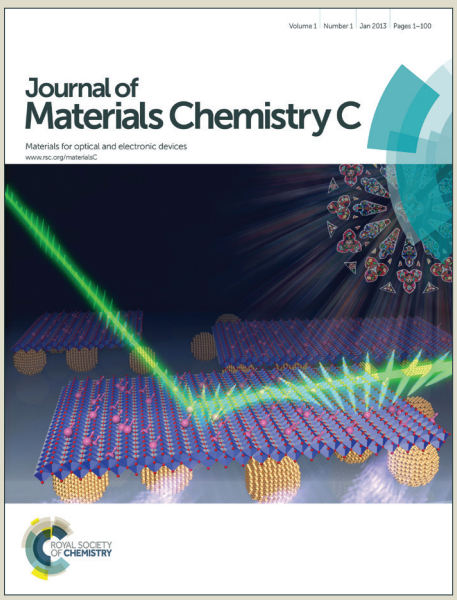

ROYAL SOCIETY OF CHEMISTRY

www.rsc.org/materialsC

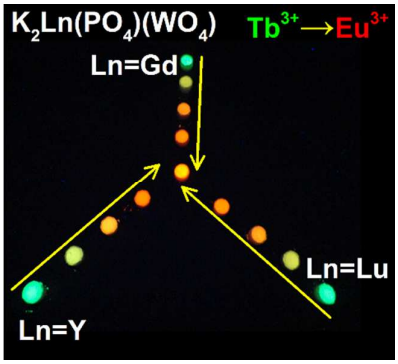

$K_2Tb_{0.5}Eu_{0.5}(PO_4)(WO_4)$ red phosphor with internal quantum efficiency of 76.45% is produced. Furthermore, the luminescence colour can be tuned from green to green by adjusting the ratio of Tb^{3+} and Eu^{3+}.

Journal of Materials Chemistry C RSCPublishing

ARTICLE

$K_2Ln(PO_4)(WO_4):Tb^{3+},Eu^{3+}$ (Ln = Y, Gd and Lu) Phosphors: Highly Efficient Pure Red and Tuneable Emission for White Light-Emitting Diodes

Cite this: DOI: 10.1039/xoxxoooooox

Received ooth January 2012,
Accepted ooth January 2012

DOI: 10.1039/xoxxoooooox

www.rsc.org/

Dawei Wen,[a] Jiajun Feng,[a] Junhao Li,[a] Jianxin Shi,[a*] Mingmei Wu,[a*] and Qiang Su[a]

A novel phosphate/tungstate family, $K_2Ln(PO_4)(WO_4)$ (Ln = Y, Gd and Lu) doped with Tb^{3+} and Eu^{3+} is synthesized via a conventional high-temperature solid-state reaction to explore new pure red phosphors with high critical concentration for white light-emitting diodes (WLEDs). The results from the Rietveld method show that the crystal structure of the hosts is composed of phosphate layers and tungstate zigzags, and the Ln^{3+}-Ln^{3+}-units are isolated by the $[PO_4]^{3-}$ groups in phosphate layers. The critical concentration of Tb^{3+} or Eu^{3+} is up to 40% - 50% in the single doped phosphors, which is ascribed to that the interaction of the isolated Ln^{3+} ions is mitigated by the $[PO_4]^{3-}$ and $[WO_4]^{2-}$ groups, so the special structure of $K_2Ln(PO_4)(WO_4)$ helps to the interaction of luminescence centres. The energy transfer from Tb^{3+} to Eu^{3+} in $K_2Ln(PO_4)(WO_4)$ is demonstrated by fluorescence decay times. By adjusting the ratio of Eu^{3+} and Tb^{3+}, we can tune the emission colour of $K_2Ln(PO_4)(WO_4):Tb^{3+}$, Eu^{3+} from green to yellow, orange and pure red. For $K_2Tb_{0.5}Eu_{0.5}(PO_4)(WO_4)$, the internal quantum efficiency of is as high as 76.45% under the excitation of 394 nm, and the emission intensity in 150°C is 92.2% of that in 25°C.

1. Introduction

Phosphor-converted white light emitting diodes (pc-WLEDs) are promising light sources due to the high electro-optical conversion efficiency, stability and reliability. There is a huge demand for novel phosphor materials with superior luminescence properties to improve the luminous efficiency.[1-7] Currently, the commercialized WLEDs fabricated by a blue LED chip with a yellow phosphor, $Y_3Al_5O_{12}:Ce^{3+}$, suffer a low colour-rendering index (CRI) and a high correlated colour temperature (CCT).[8-13] Therefore, another approach was suggested to generate white light with a combination of near-Ultraviolet (NUV) light and Red/Green/Blue (RGB) primary colour-phosphors such as $NaBaBO_3:Ce^{3+}$, a broad band green-emitting with a quantum efficiency (QE) of 58%,[14] $Na_2Y_2B_2O_7:Ce^{3+},Tb^{3+}$, generating a narrow line green emission with the QE of 75.2%,[15] $Na_xCa_{1-x}Al_{2-x}Si_{2+x}O_8:Eu^{2+}$, a blue phosphor with the external QE exceeding the commercial phosphor, $BaMgAl_{10}O_{17}:Eu^{2+},Mn^{2+}$,[16] and $Ca_4(PO_4)O:Eu^{2+}$, an efficient red phosphor.[17]

Nevertheless, the luminous efficiency of the broad band red emission is reduced due to the insensitivity of human eye in the wavelength close to the near infrared region.[18] Therefore, it is preferable to use red phosphors doped with Eu^{3+} with narrow line emission mainly in the range of 610 – 620 nm. However, the currently emitting red phosphors doped with Eu^{3+} are either inefficient under NUV excitation or deviating from red to orange: the commercial red phosphor $Y_2O_3:Eu^{3+}$ can be efficiently excited by 255 nm but has weak-line absorption of *f-f* transition in NUV region.[19] Red phosphors based on Ce^{3+}/Eu^{2+}-$(Tb^{3+})_n$-Eu^{3+} terbium bridge produce a narrow line emission with high QE under NUV excitation. In the terbium bridge phosphors, the orange line emission (590 – 600 nm, $^5D_0$-$^7F_1$) dominants, which leads to lack of red component (610 – 620 nm, $^5D_0$ - $^7F_2$). Therefore, the pure red cannot be obtained in this approach up till now.[20-22] The ratio of red and orange (R/O) emission in Eu^{3+} was investigated and the results showed that the red component increases with increasing the content of Eu^{3+}.[23] However, the metal – metal charge transition (MMCT)

effect, which quenches the emission, is enhanced as the concentration of Eu^{3+} increases in many hosts.[24-27]

In a word, to develop novel red phosphors meeting the following requirements is very urgent for NUV based WLEDs:

I. Pure red emission.

II. High conversion efficiency.

III. NUV excitation.

In order to achieve the above goal, the sensitization effect and crystal structure of the phosphor should be considered.

Recently, the sensitization effect of Tb^{3+} ions for red emitting ions, Eu^{3+}, has attracted great attention.[28-31] Tb^{3+} ions not only enhance the emission of Eu^{3+} but also broaden the absorption region due to the existence of more impurity energy levels introduced by Tb^{3+}. For instance, it was reported that Tb^{3+} ions can act as sensitizers to increase the luminescence efficiency of Eu^{3+} ions in $La_3GaGe_5O_{16}$[28] and $NaY(MoO_4)_2$[32]. What's more, the emitting colour of the phosphors is tuneable by adjusting the ratio of Tb^{3+} and Eu^{3+} ions. Therefore, it is hopeful that dual emission might be realized by this method.

Special hosts with high quenching concentration for high luminescence output are necessary. Recently, several researchers discovered that the critical concentrations of Tb^{3+} and Eu^{3+} are very high in phosphates for the reason that the luminescence centres are isolated by the surrounding $[PO_4]^{3-}$ groups. For $Ca_3Bi(PO_4)_3:Eu^{3+}$, the critical concentration of Eu^{3+} is 50%.[33] In $NaLa(PO_3)_4$, the luminescence intensity keeps increasing even though the content of Tb^{3+} or Eu^{3+} is 100% because all the rare earth sites are isolated by $[PO_4]^{3-}$.[30] This phenomenon for phosphate helps to develop red phosphors with intense excitation in NUV region. Similar to the above phosphates, the $[WO_4]^{2-}$ functional group in $Me_2Ln(PO_4)(WO_4)$ (Me = Na and K; Ln = Y, Gd and Lu) is expected to serve as a break to reduce the concentration quenching effect of luminescence centres.

So far, $Na_2Ln(PO_4)(WO_4)$ and $K_2Ho(PO_4)(WO_4)$ have been structurally characterized. In $K_2Ho(PO_4)(WO_4)$, the $[Ln^{3+}\text{-}O^{2-}Ln^{3+}]$ unit is separated by $[PO_4]^{3-}$ and $[WO_4]^{2-}$ functional groups, so that a high quenching concentration is expected in both structures.[34, 35] The vacuum ultraviolet, cathodoluminescence and up conversion were studied for $K_2Y(PO_4)(WO_4)$.[36] However, the energy transfer (ET) effect of Tb^{3+} and Eu^{3+} in $K_2Ln(PO_4)(WO_4)$ under NUV excitation is unknown, and $K_2Lu(PO_4)(WO_4)$ has never been synthesized as far as we know. Furthermore, there is no report on the potential of $K_2Ln(PO_4)(WO_4)$ phosphors for WLEDs application.

In this work, $K_2Ln(PO_4)(WO_4):Tb^{3+},Eu^{3+}$ (Ln = Y, Gd and Lu) phosphors for WLEDs are synthesized by a high temperature solid state method. The site occupation and the interaction among ions of the doped Tb^{3+} and Eu^{3+} are discussed based on the crystal structure. Luminescence properties and energy transfer of Tb^{3+} and Eu^{3+} in $K_2Ln(PO_4)(WO_4)$ are investigated. The emission colour of the phosphor can be continuously tuned from green to yellow and red by increasing the ratio of Eu^{3+}/Tb^{3+}. $K_2Tb_{0.5}Eu_{0.5}(PO_4)(WO_4)$ is found to be a novel red phosphor with high QE under NUV excitation ascribed to the special structure of $K_2Ln(PO_4)(WO_4)$ series. Finally, the temperature quenching measurement is performed to research the thermal resistance properties.

2. Experimental Section

2.1 Sample Preparation

A series of $K_2Ln_{1-x-y}Tb_xEu_y(PO_4)(WO_4)$ phosphors were synthesized by the high temperature solid-state reaction. $KHCO_3$ (A.R.), $(HN_4)_2HPO_4$ (A.R.), WO_3 (A.R.), Y_2O_3 (99.99%), Eu_2O_3 (99.99%), Gd_2O_3 (99.99%), Tb_4O_7 (99.99%) and Lu_2O_3 (99.99%) were weighed in stoichiometric ratio and ground in an agate mortar. The mixtures were first heated at 773 K for 3 h and then at 1223 K for 3 h in air atmosphere. The sintered phosphors were reground and washed with alcohol for further measurements.

2.2 Measurements and Characterizations

The powder X-ray diffraction (XRD) measurements were carried out on a D8 ADVANCE powder diffractometer with Cu K_α radiation (1.5405 Å) at room temperature. The scanning speed is 0.5°/min. The Rietveld XRD refinement is performed in Fullprof suite.[37] The photoluminescence (PL) spectra and decay curves were collected on an Edinburgh FLS920 combined fluorescence lifetime and steady state spectrometer with a 450 W xenon lamp and 60 W μF flash lamp, respectively. The temperature-dependent PL spectra were obtained on the same instrument with a temperature controller.

3. Results and Discussion

3.1 Crystal Structure of $K_2Ln(PO_4)(WO_4)$

$K_2Ho(PO_4)(WO_4)$ crystallizes in *Ibca* (NO. 70) space group and orthorhombic crystal system (ICSD-260054).[35] However, no records of $K_2Y(PO_4)(WO_4)$, $K_2Gd(PO_4)(WO_4)$ or $K_2Lu(PO_4)(WO_4)$ is available in Inorganic Crystal Structure Database (ICSD) or Joint Committee on Powder Diffraction Standards (JCPDS). Solid solutions of $K_2Ln(PO_4)(WO_4)$ (Ln = Y, Gd and Lu) may also exist due to the similar radii and valence of the rare earth ions. Here, the crystal structure data of $K_2Ho(PO_4)(WO_4)$ is used as a starting model to refine the crystal structure.[35] As presented in Figure 1, the observed and calculated patterns of $K_2Ln(PO_4)(WO_4)$ are shown with a unit cell crystal structure. Solid solutions of $K_2Ln(PO_4)(WO_4)$, which share the same structure, are formed based on the results. There is one kind of distorted site (*CN* = 8) occupied by Ln^{3+} ions in $K_2Ln(PO_4)(WO_4)$. The following description uses the unit cell crystal structure in Figure 1. The cell parameters of $K_2Ln(PO_4)(WO_4)$ are presented in Table 1 and the atomic coordinate parameters are depicted in Tables 2 - 4. It can be observed that the parameters increase as the Ln^{3+} sites are substituted by $Lu^{3+}\rightarrow Y^{3+}\rightarrow Gd^{3+}$ with the increasing radii. The expansion of crystal is due to the lager ions doping, consistent with the Vegard's law.[38, 39] The cell and atomic coordinate parameters are also presented in Figure 1, Table 1, Figure S1 and Table S1. In $K_2Ln(PO_4)(WO_4)$, the $[WO_4]^{2-}$ groups form a tungstate zigzag, which can also be regarded as two successive $[WO_4]^{2-}$ layers. The phosphate layers, formed with $[PO_4]^{3-}$ and Ln^{3+} ions, are followed by the tungstate zigzags. Therefore, the phosphate layers, as well as the Ln^{3+} ions, are isolated by the $[WO_4]^{2-}$ groups. Furthermore, the Ln^{3+}-Ln^{3+}-units are isolated

by the $[PO_4]^{3-}$ groups in phosphate layers. The special structure indicates that the interaction of the isolated Ln^{3+} ions might be obstructed. Hence, the critical concentration of the doping ions, such as Eu^{3+} and Tb^{3+}, might be high and the NUV absorption can be enhanced in this structure.

3.2 Luminescence Properties of $K_2Ln(PO_4)(WO_4):Tb^{3+}$ and $K_2Ln(PO_4)(WO_4):Eu^{3+}$

We focus on the luminescence properties of $K_2Gd(PO_4)(WO_4):Tb^{3+},Eu^{3+}$ because the properties are similar for Ln = Y, Gd, Lu when Tb^{3+} or Eu^{3+} ions are doped. The PL and PLE spectra of $K_2Gd(PO_4)(WO_4):Tb^{3+}$ and $K_2Gd(PO_4)(WO_4):Eu^{3+}$ are shown in Figure 2. Tb^{3+} ions emit green colour composed of $^5D_4$-$^7F_6$, $^5D_4$-$^7F_5$, $^5D_4$-$^7F_4$ and $^5D_4$-$^7F_3$ transitions while Eu^{3+} ions emit red colour composed of $^5D_0$-$^7F_1$, $^5D_0$-$^7F_2$, $^5D_0$-$^7F_3$ and $^5D_0$-$^7F_4$ under NUV excitation of 378 nm and 394 nm, respectively.[11, 30, 33, 40, 41] The dominant emission of Eu^{3+} originates from the electric dipole transition $^5D_0$-$^7F_2$, rather than the magnetic one$^5D_0$-$^7F_1$, indicating that Eu^{3+} ions substitute the non-inverse symmetry site in $K_2Gd(PO_4)(WO_4)$. In the PLE spectrum of $K_2Gd(PO_4)(WO_4):Tb^{3+}$, a broad band peaked at 244 nm with a shoulder at 266 nm is ascribed to the *f-d* spin allowed and forbidden transitions of Tb^{3+}, respectively. The peaks in the wavelength ranging from 300 to 500 nm are due to the *f-f* transition of Tb^{3+}. The excitation spectrum of $K_2Gd(PO_4)(WO_4):Eu^{3+}$ consists of a charge transfer band (CTB) and peaks of *f-f* transitions at 299, 319, 363, 382, 394, 418 and 466 nm being assigned to $^7F_1$–$^5H_6$, $^7F_0$–$^5H_3$, $^7F_0$–$^5D_4$, $^7F_0$–$^5L_7$, $^7F_0$–$^5L_6$, $^7F_1$–$^5D_3$ and $^7F_0$–$^5D_2$.[42-44] Here, the CTB is asymmetric, indicating it can be deconvoluted into two bands: $O^{2-}\rightarrow W^{6+}$ and $O^{2-}\rightarrow Eu^{3+}$. However, it is difficult to distinguish which is at shorter or longer wavelength.

The emission intensities as a function of Tb^{3+} or Eu^{3+} concentration in $K_2Gd(PO_4)(WO_4)$ are also shown in Figure 2. The variation trend of intensity for Tb^{3+} and Eu^{3+} is similarly composed of two regions – rapidly increasing regions (A and A') and slow decline ones (B and B'). The critical concentration is up to 40% - 50%, moreover, the concentration quenching effect is unobvious. This phenomenon is a result of the weak interaction among the luminescence centres. As mentioned in Section 3.1, the Ln^{3+}-$[PO_4]^{3-}$ layers are isolated by $[WO_4]^{2-}$ zigzags and the Ln^{3+} ions are separated by $[PO_4]^{3-}$ groups in the layers. It is probable that the mild concentration quenching effect is caused by the weak luminescence centres interactions due to the blocking of $[PO_4]^{3-}$ and $[WO_4]^{2-}$ groups in the special $K_2Ln(PO_4)(WO_4)$ structure.

The doped ions are expected to scatter randomly in the appropriate sites. Therefore, when the content is 50%, the doped luminescence ions are expected to scatter and occupy half of each double-Ln^{3+}-unit according to the law of large numbers as presented in Figure S2. It is inevitable that some double-Ln^{3+}-units are fully occupied by two luminescence ions when the content is larger than 50%. Then the interactions among ions are enhanced because there is no blocking ions group of $[PO_4]^{3-}$ or $[WO_4]^{2-}$ in such units. This site-occupy structure explanation is consistent with the observed variation trend of intensity for Tb^{3+} and Eu^{3+} in $K_2Gd(PO_4)(WO_4)$. The variation trends of intensity of Tb^{3+} and Eu^{3+} depicted in Figure S3 for $K_2Y(PO_4)(WO_4)$ and $K_2Lu(PO_4)(WO_4)$ are similar as $K_2Gd(PO_4)(WO_4)$.

3.3 Dual Emission and Energy Transfer of Tb^{3+} and Eu^{3+} in $K_2Ln(PO_4)(WO_4)$

$K_2Gd(PO_4)(WO_4):Tb^3,Eu^{3+}$ samples are chosen to investigate the ET from Tb^{3+} to Eu^{3+}. Figure 3 (a) illustrates the PL spectra of Tb^{3+}-Eu^{3+} doubly doped $K_2Gd(PO_4)(WO_4)$. The characteristic sharp line emission of Tb^{3+} and Eu^{3+} are observed. The emission intensity of Eu^{3+} ions at 616 nm increases with increasing the Eu^{3+} content, whereas the intensity of Tb^{3+} at 543 nm decreases simultaneously under 378 nm, which reflects that the energy can be transferred from Tb^{3+} to Eu^{3+} and $K_2Gd(PO_4)(WO_4):Tb^{3+},Eu^{3+}$ can be used as green-red double colour phosphors for NUV WLEDs. In Figure 3 (b), the CIE chromaticity coordinates of the corresponding samples are shifting from (0.35, 0.58) to (0.65, 0.34). More importantly, the coordinate of the red emission sample $K_2Tb_{0.5}Eu_{0.5}(PO_4)(WO_4)$ (sample V) is (0.65, 0.34), which is very close to the National Television System Committee (NTSC) standard for red subpixels (0.67, 0.33).[45] The digital photos of $K_2Ln(PO_4)(WO_4):Tb^3,Eu^{3+}$ in Figure 3 (c) also support the spectral results.

The ET from Tb^{3+} to Eu^{3+} is observed in the UV-Vis spectra.[28] Luminescence decay time measurements are performed to further analyse the ET phenomenon. As shown in Figure 4 (a), the fluorescence decay curves of $K_2Gd_{0.5-x}Tb_{0.5}(PO_4)(WO_4):xEu^{3+}$ deviate from single-exponential decay process as the concentration of Eu^{3+} ions increase. The average decay time of Tb^{3+} can be obtained from Equation (1):[29, 46]

$$\tau_{Tb} = \frac{\int_0^\infty I(t)tdt}{\int_0^\infty I(t)dt} \quad (1)$$

The values of τ_{Tb} are calculated to be 3.16, 2.38, 2.05, 1.75, 1.69 and 1.47 ms for x = 0%, 0.5%, 1%, 2%, 3% and 5% in $K_2Gd_{0.5-x}Tb_{0.5}(PO_4)(WO_4):xEu^{3+}$, and the results are presented in Figure 4 (b). It can be observed that the average time of Tb^{3+} ions decreases with the increase of Eu^{3+}, indicating the ET from Tb^{3+} to Eu^{3+}. Equation (2) can be used to estimate the Tb^{3+}-Eu^{3+} ET probability ($P_{Tb\text{-}Eu}$):[47, 48]

$$P_{Tb-Eu} = \frac{1}{\tau_x} - \frac{1}{\tau_0} \quad (2)$$

Where τ_x and τ_0 are the corresponding lifetimes of the sensitizer (Tb^{3+}) in the absence and presence of the activator (Eu^{3+}) for the same sensitizer concentration. The calculated $P_{Tb\text{-}Eu}$ values are depicted in Figure 4 (c). The ET probabilities from Tb^{3+} to Eu^{3+} increase with increasing the content of Eu^{3+}, indicating an enhanced ET process. The average decay times (τ_{Eu}) of $K_2Gd_{0.5-x}Tb_{0.5}(PO_4)(WO_4):xEu^{3+}$ are 3.30, 3.40, 3.42, 3.42 and 3.42 ms for x = 0.5%, 1%, 2%, 3% and 5% when the Eu^{3+} ions are excited by 394 nm through $^7F_0\rightarrow{}^5L_6$ transition. The values of τ_{Eu} have little change because it is still far from the critical concentration. Figure 5 illustrates the decay curves of $K_2Gd_{0.5-}$

$_x$Tb$_{0.5}$(PO$_4$)(WO$_4$):xEu^{3+}(λ_{Ex} = 378 nm, λ_{Em} = 616 nm). The different PLE spectra monitoring at 616 nm of $K_2Tb_{0.5}Eu_{0.5}(PO_4)(WO_4)$ and $K_2Gd_{0.5}Eu_{0.5}(PO_4)(WO_4)$ and the characterized Tb^{3+} transitions in Figure S4 also indicates the ET process from Tb^{3+} to Eu^{3+}. Two different processes can be observed for Eu^{3+} emission: rise-up process and decay process when excited at 378 nm. In the initial rise-up process, the energy absorbed by the $^7F_6 \rightarrow {}^5G_6$ transition in Tb^{3+} ions is transferred to Eu^{3+} ions. The rise-up process is significantly influenced by the content of Eu^{3+}. As shown in Figure 5 (a), the rise-up process becomes faster and faster with the increase of Eu^{3+} ions, which indicates that the ET process from Tb^{3+} to Eu^{3+} becomes more efficient with the increase of Eu^{3+}.

When the $K_2Gd_{0.5-x}Tb_{0.5}(PO_4)(WO_4)$:$xEu^{3+}$ samples are excited by 378 nm, the rate equations for the population densities in the $^5D_4$ level of Tb^{3+} ion and $^5D_0$ level of Eu^{3+} ion can be expressed as follows:[49, 50]

$$\frac{dN_{Tb}}{dt} = -\frac{N_{Tb}}{\tau_{Tb}} - K_{Tb-Eu}N_{Tb} \quad (3)$$

$$\frac{dN_{Eu}}{dt} = -\frac{N_{Eu}}{\tau_{Eu}} - K_{Tb-Eu}N_{Tb} \quad (4)$$

Where the N_{Tb} and N_{Eu} are the population intensities of the $^5D_4$ level of Tb^{3+} and the $^5D_0$ of Eu^{3+}, respectively. $K_{Tb\text{-}Eu}$ is the non-radiative ET rate from the $^5D_4$ state of Tb^{3+} to $^5D_0$ of Eu^{3+}. Then the fluorescence intensity $I(t)$ of Eu^{3+} ions at 616 nm under 378 nm excitation can be given as following:

$$I(t) = N_{Eu}(t) = \frac{K_{Tb-Eu}N_{Tb}}{\frac{1}{\tau_{Eu}} - \frac{1}{\tau_{Tb}}}\left[exp\left(-\frac{t}{\tau_{Tb}}\right) - exp\left(-\frac{t}{\tau_{Eu}}\right)\right] \quad (5)$$

Using the measured values of τ_{Tb} and τ_{Eu}, the simulation curves for the $K_2Gd_{0.5-x}Tb_{0.5}(PO_4)(WO_4)$:$xEu^{3+}$ samples are obtained as presented in Figure 5 (b), which show two process for Eu^{3+} emission, being similar to the measured curves. That is to say, the theoretical results are consistent with the experimental observations.

3.4 Performance Tests of the $K_2Tb_{0.5}Eu_{0.5}(PO_4)(WO_4)$ Phosphors

The relative integrated emission intensity of $K_2Tb_{0.5}Eu_{0.5}(PO_4)(WO_4)$, $K_2Gd_{0.5}Eu_{0.5}(PO_4)(WO_4)$, $K_2Lu_{0.5}Eu_{0.5}(PO_4)(WO_4)$ and $K_2Y_{0.5}Eu_{0.5}(PO_4)(WO_4)$ is 100%, 90.1%, 74.7% and 72.9%, respectively, under the excitation of 394 nm. Therefore, we choose the best one for quantum efficiency (QE) test. The (QE) of the $K_2Tb_{0.5}Eu_{0.5}(PO_4)(WO_4)$ phosphor was measured by the integrated sphere method at room temperature under the excitation of 394 nm.[51, 52] From Figure 5S, the value of QE (Φ) can be calculated by the following equation:[15, 53]

$$\Phi = \frac{\int L_S}{\int E_R - \int E_S} \quad (6)$$

Where $\int L_S$ is the integrated intensity of the PL spectrum for the sample, and $\int E_R$ and $\int E_S$ are the integrated intensity of the PLE spectra for $BaSO_4$ powder and the sample, respectively. The internal QE (IQE) of $K_2Tb_{0.5}Eu_{0.5}(PO_4)(WO_4)$ at room temperature is measured to be 76.45% under the excitation of 394 nm, while the external QE (EQE) is 35.2%. This result is compared with the reported red emitting phosphors in Table 5.[20, 54-57] The IQE of $K_2Tb_{0.5}Eu_{0.5}(PO_4)(WO_4)$ is a little lower than that of $Na_2Y_2B_2O_7$:Ce^{3+},Tb^{3+},Eu^{3+} and $Sr_2Si_5N_8$:Eu^{2+} but far better than that of Y_2O_3:Eu^{3+} and Y_2O_2S:Eu^{3+}. Furthermore, the dominant emission transition of phosphors with Ce^{3+}-$(Tb^{3+})_n$-Eu^{3+} is $^5D_0 \rightarrow {}^7F_1$ (magnetic dipole transition). This type of phosphors emits orange colour due to the dominant magnetic dipole transition. The harsh synthesis conditions of nitrides increases the cost. Therefore, the $K_2Tb_{0.5}Eu_{0.5}(PO_4)(WO_4)$ phosphor has certain advantages over the reported ones previously. In Figure 6, the PL spectra of $K_2Tb_{0.5}$-$Eu_{0.5}(PO_4)(WO_4)$ and Y_2O_3:Eu^{3+} under 394 nm show obvious disparity, being consistent with the QE measurement and the references.

The special structure of $K_2Ln(PO_4)(WO_4)$ with $[WO_4]^{2-}$ and $[PO_4]^{3-}$ blocking functional groups weakens the interaction of the luminescence centres. Hence, the critical concentrations of Eu^{3+} and Tb^{3+} is high and the luminescence intensity is promising at room temperature.

Temperature dependence PL intensities were collected in the range of 25°C to 150°C. In Figure 7, it is observed that the integrated intensities of $K_2Tb_{0.5}Eu_{0.5}(PO_4)(WO_4)$ phosphor decrease with increasing the temperature. The integrated emission intensity at 150°C is 92.2% of that at room temperature, demonstrating the good thermal quenching properties of $K_2Tb_{0.5}Eu_{0.5}(PO_4)(WO_4)$ phosphor. The thermal stability might be ascribed to the lower phonon interaction of the host. This result is better than the red phosphors $LaMgAl_{11}O_{19}$:Sm^{3+},Eu^{3+} (~60%) and α-Ca_2SiO_4:Eu^{2+} (~40%).[58, 59] Arrhenius equation is fitted to the thermal quenching data of $K_2Tb_{0.5}Eu_{0.5}(PO_4)(WO_4)$ phosphor to understand the activation energy and the temperature dependence of emission intensity:[60]

$$I = \frac{I_0}{1 + Aexp\left(-\frac{\Delta E}{kT}\right)} \quad (7)$$

Where I_0 is the initial emission intensity, I is the intensity at different temperatures, ΔE is activation energy of thermal quenching, A is a constant for a certain host and k is the Boltzmann constant (8.617×10^{-5}eV). Equation (7) can be revised as:

$$-\frac{\Delta E}{kT} + \ln A = ln\left(\frac{I_0}{I} - 1\right) \quad (8)$$

The activation energy ΔE is calculated to be 0.19 eV according to the fitting result in Figure 7 (b).

Conclusions

In summary, $K_2Ln(PO_4)(WO_4)$:Tb^{3+},Eu^{3+} (Ln = Y,Gd and Lu) phosphors have been synthesized by using high temperature solid state reaction method. The critical concentration of Tb^{3+} or Eu^{3+} is up to 40% - 50% in the single doped phosphor ascribed to the special structure of $K_2Ln(PO_4)(WO_4)$. Energy transfer from Tb^{3+} to Eu^{3+} has been investigated while the piecewise decay observed and fitting curves are obtained. The emission colour of $K_2Ln(PO_4)(WO_4)$:Tb^{3+}, Eu^{3+} can be green, green-red double or pure red by adjusting the ratio of Eu^{3+} and Tb^{3+}. The IQE and EQE of $K_2Tb_{0.5}Eu_{0.5}(PO_4)(WO_4)$ phosphor is 76.45% and 35.24%, respectively. The thermal quenching property has been investigated in detail and the corresponding activation energy is obtained to be about 0.19 eV from

Arrhenius equation. The highly photoluminescent efficiency and the excellently thermal quenching property make $K_2Tb_{0.5}Eu_{0.5}(PO_4)(WO_4)$ to be a promising pure red phosphor for application in near-ultraviolet WLEDs.

Acknowledgements

This work was financially supported by grants from the Joint Funds of the National Natural Science Foundation of China and Guangdong Province(No. U1301242), Research Fund for the Doctoral Program of Higher Education of China (RFDP) (No. 20130171130001), and the Natural Science Foundation of Guangdong Province (No.9151027501000047).

Notes and references

[a]Address: MOE Key Laboratory of Bioinorganic and Synthetic Chemistry/State Key Laboratory of Optoelectronic Materials and Technology, Key Laboratory of Environment andEnergy Chemistry of Guangdong Higher Education Institutes, School of Chemistry and Chemical Engineering, Sun Yat-Sen University, No. 135, Xin Gang Xi Road, Guangzhou 510275, P.R. China.Electronic Supplementary Information (ESI) available: [details of any supplementary information available should be included here]. See DOI: 10.1039/b000000x/

1 C. C. Lin and R.-S. Liu, *J. Phys. Chem. Lett.*, 2011, **2**, 1268-1277.
2 H. A. Höppe, *Angew. Chem. Int. Ed.*, 2009, **48**, 3572-3582.
3 M. Shang, C. Li and J. Lin, *Chem. Soc. Rev.*, 2014, **43**, 1372-1386.
4 C. Feldmann, T. Jüstel, C. R. Ronda and P. J. Schmidt, *Adv. Funct. Mater.*, 2003, **13**, 511-516.
5 R.-J. Xie, N. Hirosaki, T. Suehiro, F.-F. Xu and M. Mitomo, *Chem. Mater.*, 2006, **18**, 5578-5583.
6 X. Gong, J. Huang, Y. Chen, Y. Lin, Z. Luo and Y. Huang, *Inorg. Chem.*, 2014, **53**, 6607-6614.
7 J. Yan, L. Ning, Y. Huang, C. Liu, D. Hou, B. Zhang, Y. Huang, Y. Tao and H. Liang, *J. Mater. Chem. C*, 2014, **2**, 8328-8332.
8 X. Chen, P. Dai, X. Zhang, C. Li, S. Lu, X. Wang, Y. Jia and Y. Liu, *Inorg. Chem.*, 2014, **53**, 3441-3448.
9 K. Li, D. Geng, M. Shang, Y. Zhang, H. Lian and J. Lin, *J. Phys. Chem. C*, 2014, **118**, 11026-11034.
10 N. Guo, H. You, C. Jia, R. Ouyang and D. Wu, *Dalton Trans.*, 2014, **43**, 12373-12379.
11 D. Wen, G. Yang, H. Yang, J. Shi, M. Gong and M. Wu, *Mater. Lett.*, 2014, **125**, 63-66.
12 D. Geng, K. Li, H. Lian, M. Shang, Y. Zhang, Z. Wu and J. Lin, *Eur. J. Inorg. Chem.*, 2014, **2014**, 1955-1964.
13 Z. Tao, W. Zhang, L. Qin, Y. Huang, D. Wei and H. J. Seo, *J. Alloys Compd.*, 2014, **588**, 540-545.
14 R. Yu, S. Zhong, N. Xue, H. Li and H. Ma, *Dalton Trans.*, 2014, **43**, 10969-10976.
15 D. Wen, H. Yang, G. Yang, J. Shi, M. Wu and Q. Su, *J. Solid State Chem.*, 2014, **213**, 65-71.
16 G.-y. Lee, J. Y. Han, W. B. Im, S. H. Cheong and D. Y. Jeon, *Inorg. Chem.*, 2012, **51**, 10688-10694.
17 D. Deng, H. Yu, Y. Li, Y. Hua, G. Jia, S. Zhao, H. Wang, L. Huang, Y. Li, C. Li and S. Xu, *J. Mater. Chem. C*, 2013, **1**, 3194-3199.
18 P. S. Dutta and A. Khanna, *ECS J. Solid State Sci. Technol.*, 2013, **2**, R3153-R3167.
19 J.-G. Li, X. Li, X. Sun and T. Ishigaki, *J. Phys. Chem. C*, 2008, **112**, 11707-11716.
20 Z. Xia, J. Zhuang and L. Liao, *Inorg. Chem.*, 2012, **51**, 7202-7209.
21 Y. Jia, W. Lu, N. Guo, W. Lu, Q. Zhao and H. You, *Phys. Chem. Chem. Phys.*, 2013, **15**, 13810-13813.
22 A. A. Setlur, *Electrochem. Solid-State Lett.*, 2012, **15**, J25-J27.
23 S. Sohal, M. Nazari, X. Zhang, E. Hassanzadeh, V. V. Kuryatkov, J. Chaudhuri, L. J. Hope-Weeks, J. Y. Huang and M. Holtz, *J. Appl. Phys.*, 2014, **115**, 183505.
24 G. Blasse and A. Bril, *J. Chem. Phys.*, 1967, **47**, 1920-1926.
25 K. C. Bleijenberg and G. Blasse, *J. Solid State Chem.*, 1979, **28**, 303-307.
26 G. Blasse, *Phys. Status Solidi A*, 1983, **75**, K41-K43.
27 Y. Jia, W. Lu, N. Guo, W. Lu, Q. Zhao and H. You, *Chem. Commun.*, 2013, **49**, 2664-2666.
28 J. Zhou and Z. Xia, *J. Mater. Chem. C*, 2014, **2**, 6978-6984.
29 D. Wen, J. Shi, M. Wu and Q. Su, *ACS Appl. Mater. Interfaces*, 2014, **6**, 10792-10801.
30 C. Liu, D. Hou, J. Yan, L. Zhou, X. Kuang, H. Liang, Y. Huang, B. Zhang and Y. Tao, *J. Phys. Chem. C*, 2014, **118**, 3220-3229.
31 M. O. Rodrigues, J. D. L. Dutra, L. A. O. Nunes, G. F. de Sá, W. M. de Azevedo, P. Silva, F. A. A. Paz, R. O. Freire and S. A. Júnior, *J. Phys. Chem. C*, 2012, **116**, 19951-19957.
32 Z. Xu, C. Li, G. Li, R. Chai, C. Peng, D. Yang and J. Lin, *J. Phys. Chem. C*, 2010, **114**, 2573-2582.
33 M. Jiao, N. Guo, W. Lu, Y. Jia, W. Lv, Q. Zhao, B. Shao and H. You, *Dalton Trans.*, 2013, **42**, 12395-12402.
34 M. Daub, A. J. Lehner and H. A. Hoppe, *Dalton Trans.*, 2012, **41**, 12121-12128.
35 K. V. Terebilenko, I. V. Zatovsky, V. N. Baumer, N. S. Slobodyanik and O. V. Shishkin, *Acta Crystallogr., Sect. E: Struct. Rep. Online*, 2008, **64**, i75.
36 L. Han, L. Zhao, J. Zhang, Y. Wang, L. Guo and Y. Wang, *RSC Adv.*, 2013, **3**, 21824-21831.
37 J. Rodríguez-Carvajal, *Physica B*, 1993, **192**, 55-69.
38 S.-P. Lee, C.-H. Huang, T.-S. Chan and T.-M. Chen, *ACS Appl. Mater. Interfaces*, 2014, **6**, 7260-7267.
39 J. Park, S. J. Lee and Y. J. Kim, *Cryst. Growth Des.*, 2013, **13**, 5204-5210.
40 Z. Xia, Y. Liang, D. Yu, M. Zhang, W. Huang, M. Tong, J. Wu and J. Zhao, *Opt. Laser Technol.*, 2014, **56**, 387-392.
41 L. Wang, J. Dong, P. Huang and C. E. Cui, *J. Alloys Compd.*, 2014, **589**, 330-335.
42 J. Wang, Y. Cheng, Y. Huang, P. Cai, S. I. Kim and H. J. Seo, *J. Mater. Chem. C*, 2014, **2**, 5559-5569.
43 G. Zhu, Z. Ci, Y. Shi, M. Que, Q. Wang and Y. Wang, *J. Mater. Chem. C*, 2013, **1**, 5960-5969.
44 N. Zhang, C. Guo, J. Zheng, X. Su and J. Zhao, *J. Mater. Chem. C*, 2014, **2**, 3988-3994.
45 X. Ye, D. Wu, M. Yang, Q. Li, X. Huang, Y. Yang and H. Nie, *ECS J. Solid State Sci. Technol.*, 2014, **3**, R95-R99.
46 G. Blasse, *Philips Res. Rep.*, 1969, **34**, P131.
47 M. Xie, Y. Tao, Y. Huang, H. Liang and Q. Su, *Inorg. Chem.*, 2010, **49**, 11317-11324.
48 Y.-C. Li, Y.-H. Chang, Y.-S. Chang, Y.-J. Lin and C.-H. Laing, *J. Phys. Chem. C*, 2007, **111**, 10682-10688.
49 D. Hou, H. Liang, M. Xie, X. Ding, J. Zhong, Q. Su, Y. Tao, Y. Huang and Z. Gao, *Opt. Express*, 2011, **19**, 11071-11083.
50 C. Zhang, H. Liang, S. Zhang, C. Liu, D. Hou, L. Zhou, G. Zhang and J. Shi, *J. Phys. Chem. C*, 2012, **116**, 15932-15937.
51 W.-R. Liu, C.-H. Huang, C.-P. Wu, Y.-C. Chiu, Y.-T. Yeh and T.-M. Chen, *J. Mater. Chem.*, 2011, **21**, 6869-6874.
52 Z. Tao, Y. Huang and H. J. Seo, *Dalton Trans.*, 2013, **42**, 2121-2129.
53 Z. Xia, R.-S. Liu, K.-W. Huang and V. Drozd, *J. Mater. Chem.*, 2012, **22**, 15183-15189.
54 J. Hou, X. Yin, Y. Fang, F. Huang and W. Jiang, *Opt. Mater.*, 2012, **34**, 1394-1397.
55 Y. Huang, Y. Nakai, T. Tsuboi and H. J. Seo, *Opt. Express*, 2011, **19**, 6303-6311.
56 D. Wen and J. Shi, *Dalton Trans.*, 2013, **42**, 16621-16629.
57 R.-J. Xie, N. Hirosaki, N. Kimura, K. Sakuma and M. Mitomo, *Appl. Phys. Lett.*, 2007, **90**, 191101.
58 X. Min, Z. Huang, M. Fang, Y.-G. Liu, C. Tang and X. Wu, *Inorg. Chem.*, 2014, **53**, 6060-6065.
59 Y. Sato, H. Kato, M. Kobayashi, T. Masaki, D.-H. Yoon and M. Kakihana, *Angew. Chem. Int. Ed.*, 2014, **53**, 7756-7759.
60 S. Bhushan and M. V. Chukichev, *J. Mater. Sci. Lett.*, 1988, **7**, 319-321.

Table 1. Cell parameters of $K_2Ln(PO_4)(WO_4)$

Ln	**Radii of Ln^{3+} when *CN* = 8**	**Cell Parameters of $K_2Ln(PO_4)(WO_4)$**
		$\alpha=\beta=\gamma=90°$
Y	1.019 Å	a=6.87(6)Å, b=12.15(3)Å, c=19.72(0)Å, V=1647.99(0)Å^3
Gd	1.053 Å	a=6.96(8)Å, b=12.28(5) Å, c=19.75(7)Å, V=1691.40(0)Å^3
Lu	0.977Å	a=6.80(6)Å, b=12.06(1) Å, c=19.69(1)Å, V=1616.29(0)Å^3

Table 2. Refined atomic coordinate parameters for $K_2Y(PO_4)(WO_4)$

Atom	Wyck.	x/a	y/b	z/c
W1	8e	0.500(0)	0.250(0)	0.334(5)
Y1	8d	0.750(0)	0.325(1)	0.500(0)
K1	16f	0.970(6)	0.069(7)	0.343(8)
P1	8d	0.750(0)	0.072(6)	0.500(0)
O1	16f	0.770(3)	0.302(6)	0.385(4)
O2	16f	0.442(0)	0.364(3)	0.284(9)
O3	16f	0.730(8)	-0.004(7)	0.438(3)
O4	16f	0.922(9)	0.142(4)	0.492(2)

Table 3. Refined atomic coordinate parameters for $K_2Gd(PO_4)(WO_4)$

Atom	Wyck	x/a	y/b	z/c
W1	8e	0.500(0)	0.250(0)	0.332(6)
Gd1	8d	0.750(0)	0.324(6)	0.500(0)
K1	16f	0.970(1)	0.073(2)	0.344(8)
P1	8d	0.750(0)	0.070(4)	0.500(0)
O1	16f	1.507(6)	0.400(7)	0.318(2)
O2	16f	0.412(0)	0.310(0)	0.318(6)
O3	16f	0.691(0)	-0.006(5)	0.434(6)
O4	16f	0.928(4)	0.154(2)	0.488(9)

Table 4. Refined atomic coordinate parameters for $K_2Lu(PO_4)(WO_4)$

Atom	Wyck	x/a	y/b	z/c
W1	8e	0.500(0)	0.250(0)	0.336(0)
Lu1	8d	0.750(0)	0.325(8)	0.500(0)
K1	16f	0.968(7)	0.079(9)	0.343(9)
P1	8d	0.750(0)	0.070(4)	0.500(0)
O1	16f	0.700(7)	0.293(6)	0.398(6)
O2	16f	0.442(0)	0.364(3)	0.328(0)
O3	16f	0.745(1)	0.004(6)	0.438(3)
O4	16f	0.922(9)	0.151(4)	0.477(5)

Table 5. The IQE values of $K_2Tb_{0.5}Eu_{0.5}(PO_4)(WO_4)$ and some reported red phosphors

Sample	IQE	Chromaticity	Note
$K_2Tb_{0.5}Eu_{0.5}(PO_4)(WO_4)$	76.4%	Red	This Work
$Y_2O_3:Eu^{3+}$	72.5%	Red	Ref 49
$Y_2O_2S:Eu^{3+}$	35%	Red	Ref 50
$Na_2Y_2B_2O_7:Ce^{3+},Tb^{3+},Eu^{3+}$	77%	Orange	Ref 51
$Ba_2Tb(BO_3)_2Cl:Eu^{2+},Eu^{3+}$	56%	Orange	Ref 18
$Sr_2Si_5N_8:Eu^{2+}$	79%	Red	Ref 52

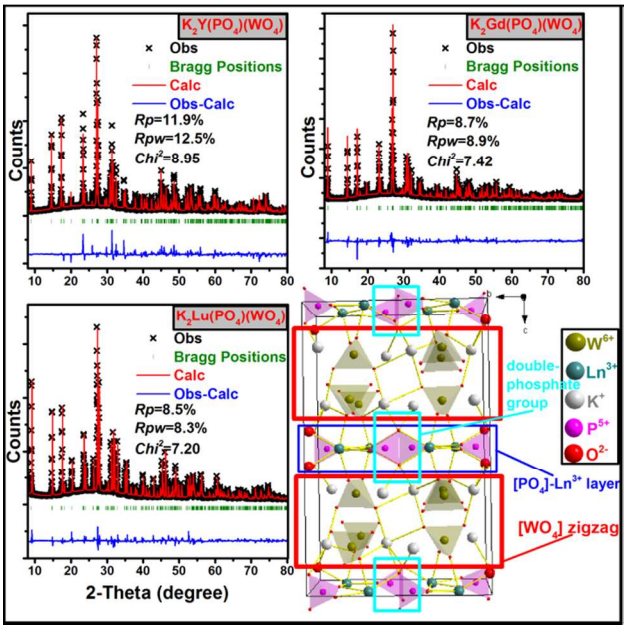

Figure 1. The calculated, observed XRD patterns, residual curves and crystal structure of $K_2Ln(PO_4)(WO_4)$ (Ln = Y, Gd and Lu).

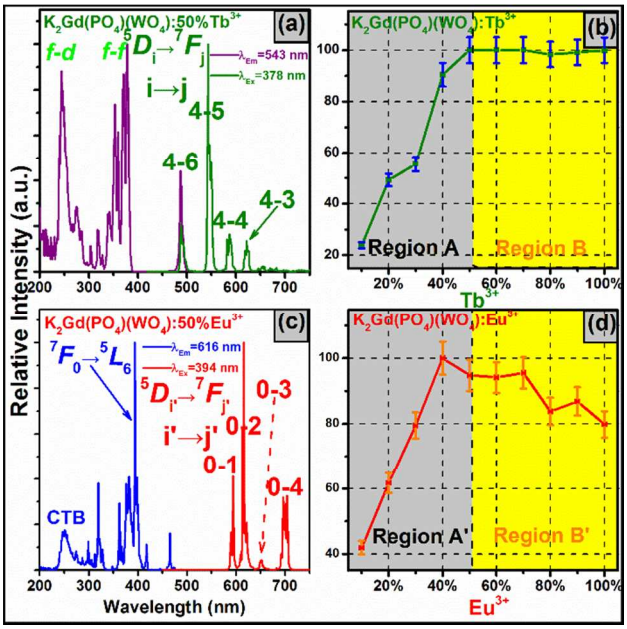

Figure 2. Photoluminescence and excitation spectra of $K_2Gd(PO_4)(WO_4):Tb^{3+}$, $K_2Gd(PO_4)(WO_4):Eu^{3+}$ and the emission intensity as a function of Tb^{3+} or Eu^{3+} concentration. (Standard error for the measurements is ± 5%)

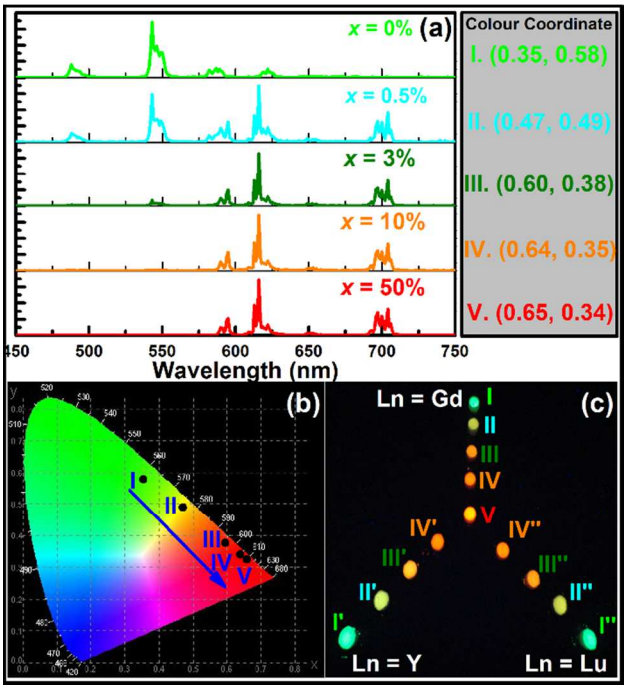

Figure 3. Photoluminescence spectra of $K_2Gd_{0.5-x}Tb_{0.5}(PO_4)(WO_4):xEu^{3+}$ (x = 0%, 0.5%, 3%, 10% and 50%, respectively) (a), the corresponding colour coordinates under 378 nm excitation (b) and the digital photos of $K_2Ln_{0.5-x}Tb_{0.5}(PO_4)(WO_4):xEu^{3+}$ samples under 365 nm UV lamp (c).

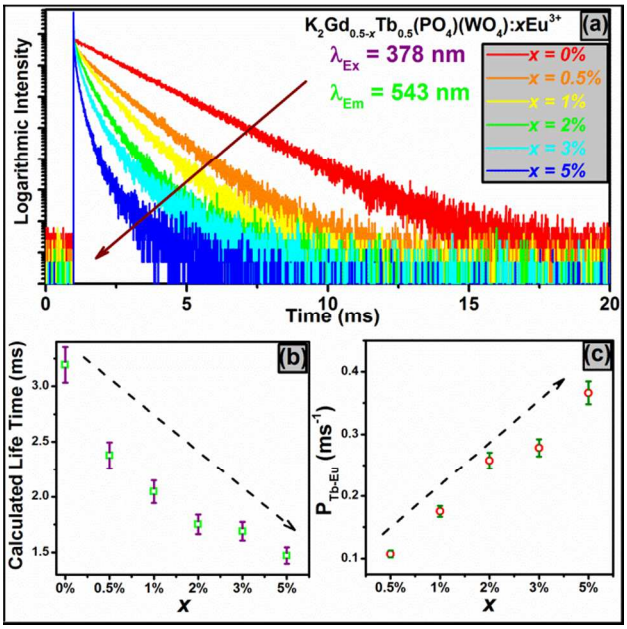

Figure 4. Decay curves (a), fluorescence lifetimes of Tb^{3+} and energy transfer probability $P_{Tb\text{-}Eu}$ as a function of x value in $K_2Gd_{0.5-x}Tb_{0.5}(PO_4)(WO_4):xEu^{3+}$. (Standard error for the measurements is ± 5%)

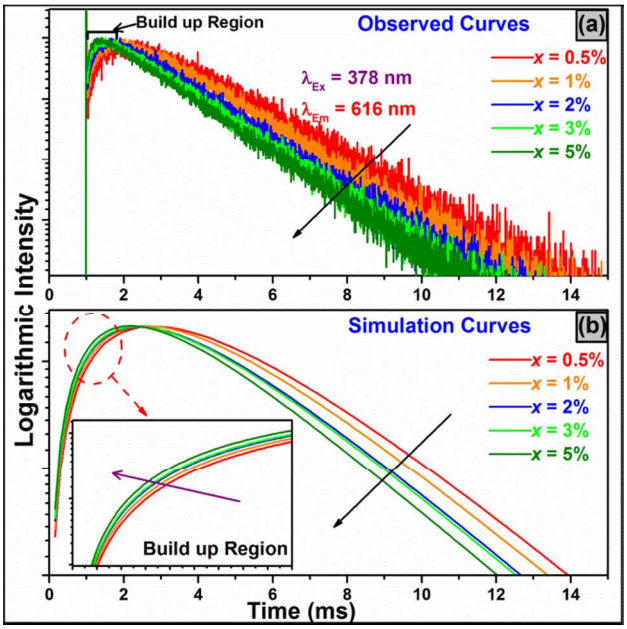

Figure 5. Fluorescence decay curves for $K_2Gd_{0.5-x}Tb_{0.5}(PO_4)(WO_4):xEu^{3+}$ (a) and the corresponding simulation curves (b).

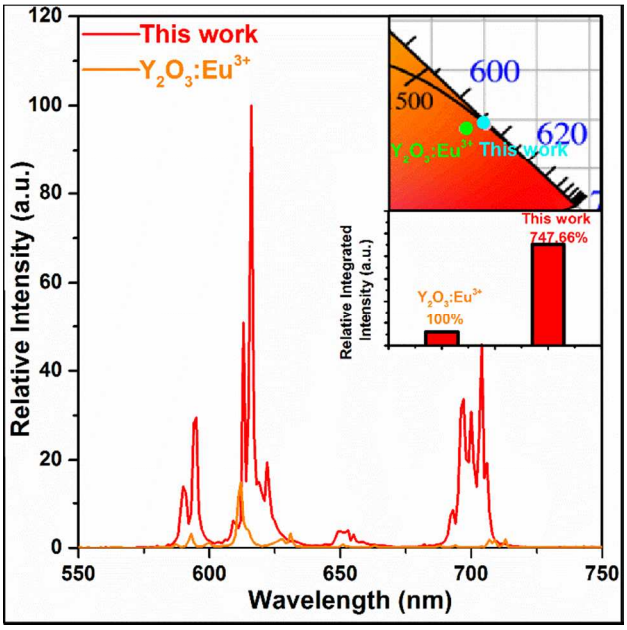

Figure 6. Comparison of the PL spectra of $K_2Tb_{0.5}Eu_{0.5}(PO_4)(WO_4)$ and $Y_2O_3:Eu^{3+}$ under 394 nm excitation and the corresponding chromaticity coordinates.

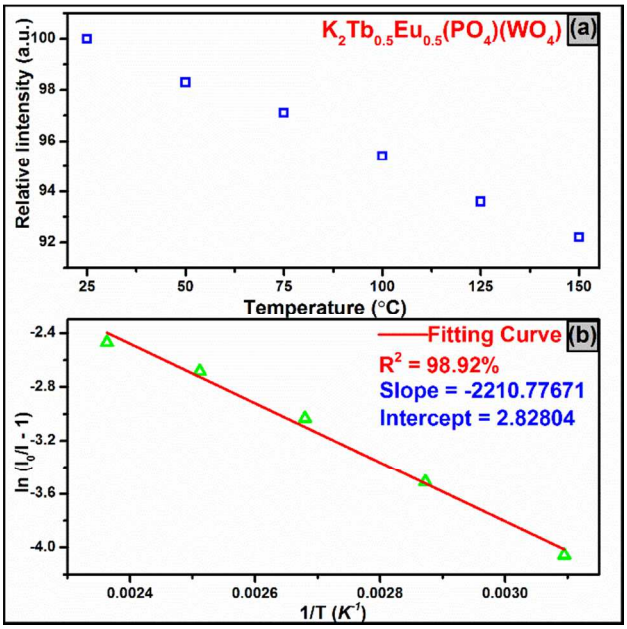

Figure 7. Temperature dependence of the emission integrated intensity of $K_2Tb_{0.5}Eu_{0.5}(PO_4)(WO_4)$ (a) and the Arrherrius fitting result (b).